ACS OMEGA

Open Access

http://pubs.acs.org/journal/acsodf

Article

Nitroreductase-Responsive Fluorescent "Off-On" Photosensitizer for Hypoxic Tumor Imaging and Dual-Modal Therapy

Dan Shen,[‖] Shangli Ding,[‖] Quan Lu, Zhengjun Chen, Ling Chen, Jiajia Lv, Jie Gao,* and Zeli Yuan*

Cite This: *ACS Omega* 2024, 9, 30685−30697

Read Online

ACCESS | Metrics & More | Article Recommendations | Supporting Information

ABSTRACT: Photothermal therapy synergized with photodynamic therapy for the treatment of tumors has emerged as a promising strategy. However, designing photosensitizers with both high photothermal efficiency and high photodynamic performance remains challenging. In contrast, the strategy of rationalizing the design of photosensitizers using the physiological properties of tumors to improve the photon utilization of photosensitizers during phototherapy is more advantageous than the approach of endowing a single photosensitizer with complex functions. Herein, we propose a molecular design (CyNP) to convert from photothermal therapy to photodynamic synergistic photothermal therapy based on the prevalent properties of hypoxic tumors. In the normoxic region of tumors, the deactivation pathway of CyNP excited state is mainly the conversion of photon energy to thermal energy; in the hypoxic region of tumors, CyNP is reduced to CyNH by nitroreductase, and the deactivation pathway mainly includes radiation leap, energy transfer between CyNP and oxygen, and conversion of photons energy to heat energy. This strategy enables real-time fluorescence detection of hypoxic tumors, and it also provides dual-mode treatment for photothermal and photodynamic therapy of tumors, achieving good therapeutic effects in vivo tumor treatment. Our study achieves more efficient tumor photoablation and provides a reference for the design ideas of smart photosensitizers.

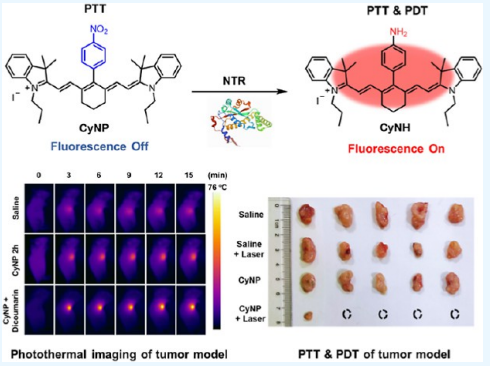

1. INTRODUCTION

Cancer remains a crucial disease of global concern, and the evolution of cancer diagnostic and therapeutic technologies has been a serious challenge that scientists urgently need to address.[1−3] Among various diagnostic and therapeutic techniques, optical diagnostic and therapeutic techniques based on photosensitizers (PSs), such as fluorescence imaging combined with photodynamic therapy (PDT) and photothermal therapy (PTT), are powerful tools for real-time diagnosis and in situ treatment due to their precise spatial and temporal selectivity, minimal invasiveness, and negligible systemic toxicity, showing greater advantages than conventional treatments (chemotherapy and surgery) in achieving real-time diagnosis and in situ treatment.[4−6] PDT utilizes PSs to transfer energy to the surrounding oxygen, which results in the production of highly energetic singlet oxygen ($^1O_2$) and acts on biological macromolecules, which undergoes an oxidative reaction that in turn damages the cells or even kills them.[7−9] The principle of PTT is to use a photothermal agent to convert photon energy into heat, cause local hyperthermia, and ultimately kill tumor cells through apoptotic and necrotic pathways.[10−12] Although phototherapy represented by PDT or PTT has gained significant momentum in the precision treatment of tumors, a single phototherapy modality also shows limitations due to the specific microenvironment of tumors.[13−15] For example, the local oxygen content of the tumor largely influences the efficacy of PDT, and the hypoxic nature of tumors restricts the effective treatment of hypoxic tumors by PDT.[16,17] Meanwhile, few photothermal agents can simultaneously meet the high absorption coefficient, weak fluorescence quantum yield, and weak $^1O_2$ yield, which are the key conditions for making photothermal agents with high photothermal efficiency.[18,19] Moreover, the heat shock effect produced by tumor stress on PTT also inhibits the therapeutic effect of PTT to some extent.[20−22] Therefore, researchers increasingly favor a synergistic treatment strategy of both than a single PDT or PTT phototherapeutic modality.

Most PSs such as IR780, BODIPY, and ICG exhibit both PDT and PTT properties as well as excellent fluorescence imaging performance,[23−26] which is determined by the structure of the PS and its complex energy dissipation pathways. After absorbing photon energy, PSs leap from the ground state to the excited state, and the excited state of PSs undergo two main energy deactivation processes: (1) fluorescence generation via the radiative leap pathway; (2) nonradiative leap pathways to convert energy to heat or to

Received: April 1, 2024
Revised: June 27, 2024
Accepted: July 2, 2024
Published: July 7, 2024

Scheme 1. (a) Schematic Diagram of the Structure and Mechanism of Conversion of CyNP to Its Reduction Product. (b) Schematic Diagram of CyNP and Its Reduction Product for Photoablation of Tumors

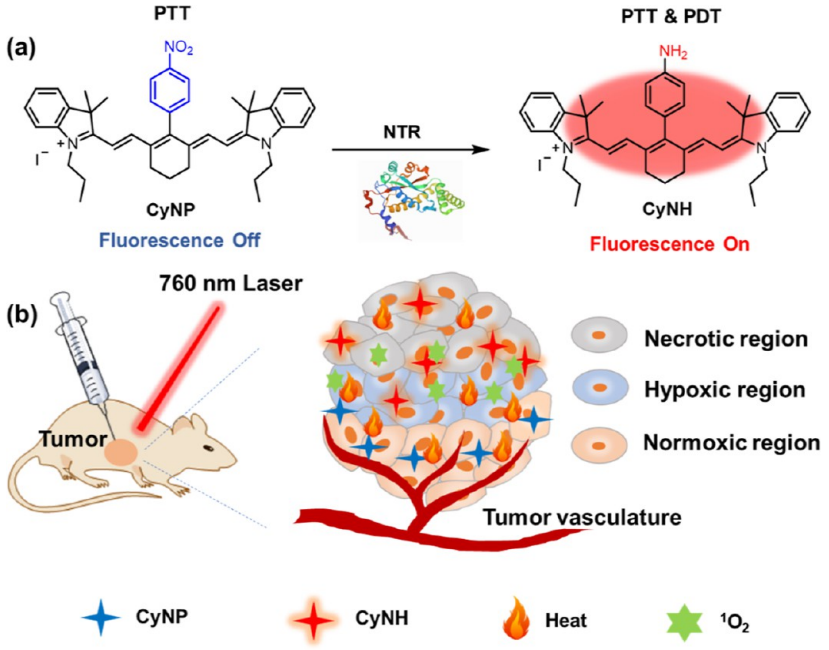

oxygen to produce ROS and/or phosphorescence (intersystem crossing).[27−29] The photon energy absorbed by PS is constant, and there is often competition between various energy dissipation pathways,[18,19] making the design of PS with both fluorescence imaging diagnostics and high photothermal conversion efficiency as well as high production of active oxygen a challenging task. Therefore, flexible strategies are urgently needed to achieve efficient PDT cooperation with PTT for tumor optical diagnostic and therapeutic techniques.

Here, we propose a smart molecular design (CyNP) for near-infrared (NIR) fluorescence imaging to detect hypoxic tumors and PTT cooperative PDT for enhancing tumor phototherapy (Scheme 1a). CyNP uses the NIR absorbing and emitting (>700 nm) cyanine molecule IR780 as the PS core structure, and CyNP is obtained by replacing the chlorine atom of the central carbon of IR780 with a nitrobenzene group. CyNP is induced by the introduction of the nitrobenzene group to produce a photoinduced electron transfer effect (PET) which quenches its fluorescence. At this time, under 760 nm radiation, CyNP in the excited state mainly releases energy to generate photothermal heat through the nonradiative leap pathway, which ablates the tumor through high temperature (Scheme 1b). There are regions with different oxygen concentrations inside the tumor, and as the degree of hypoxia within the tumor deepens, the nitroreductase level is constantly upregulated.[30,31] Nitroreductase reduces CyNP to the same skeleton molecule CyNH (Scheme 1a), and its excited state inactivation pathway includes radiative and nonradiative leaps. When CyNH fluorescence is restored, it also generates photodynamic and photothermal properties under 760 nm radiation (Scheme 1b).

2. RESULTS AND DISCUSSION

2.1. Design and Synthesis of the CyNP. IR780 is a class of small NIR molecules containing nitrogen heterocycles at both ends and connected by multiple hypomethyl-long conjugated chains in the middle. The selection of IR780 as the primary core for the PS in this study was based on its exceptional extinction coefficient and robust fluorescence in the NIR range, which is effective in generating ROS and photothermal heat under NIR light radiation for cancer therapy.[32,33] Many studies have reported that nitroaryl groups can be used as electron acceptors to design fluorescent probes for PET mechanism,[30,34−37] and in our previous work a PET effect PS was also constructed for tumor therapy using nitrobenzyl.[38] The PET phenomenon can partially suppress the fluorescence and generation of $^1O_2$ by the PS, redirecting most of the absorbed photon energy toward thermal energy conversion. This approach represents a crucial tactic in developing photothermal agents with enhanced efficiency in converting light into heat. Hypoxia is a common feature observed in solid tumors, with the majority of these tumors having an average oxygen concentration of 4% and potentially dropping as low as 0%.[30,39] In hypoxic tumor cells, changes in their internal environment such as low oxygen partial pressure, weakly acidic system, and enhanced reducing ability cause overexpression of some reductase lines, such as nitroreductase (NTR),[40,41] whose concentration levels directly correlate with the degree of tumor hypoxia. NTR can utilize reduced nicotinamide purine dinucleotide/reduced nicotinamide purine dinucleotide phosphate [NAD(P)H] for the reductive metabolism of nitroaromatic compounds and nitroheterocyclic derivatives. Nitro compounds are catalyzed by NTR, supplied with electrons by NAD(P)H, and undergo single electron transfer to generate nitro anion radicals, which are further reduced to hydroxylamines or amino groups.[42−44] Therefore, we used a NTR specifically expressed by the hypoxic tumor as a switch to reduce CyNP to amino-bearing CyNH, and its excited state deactivation pathway was changed. With this strategy, we have flexibly implemented NIR fluorescence imaging for the detection of hypoxic tumors while concurrently employing PTT and PDT in combination for tumor phototherapy. Therefore, CyNP and CyNH were obtained by one-step synthesis via Suzuki−Miyaura reaction using

https://doi.org/10.1021/acsomega.4c03098
ACS Omega 2024, 9, 30685−30697

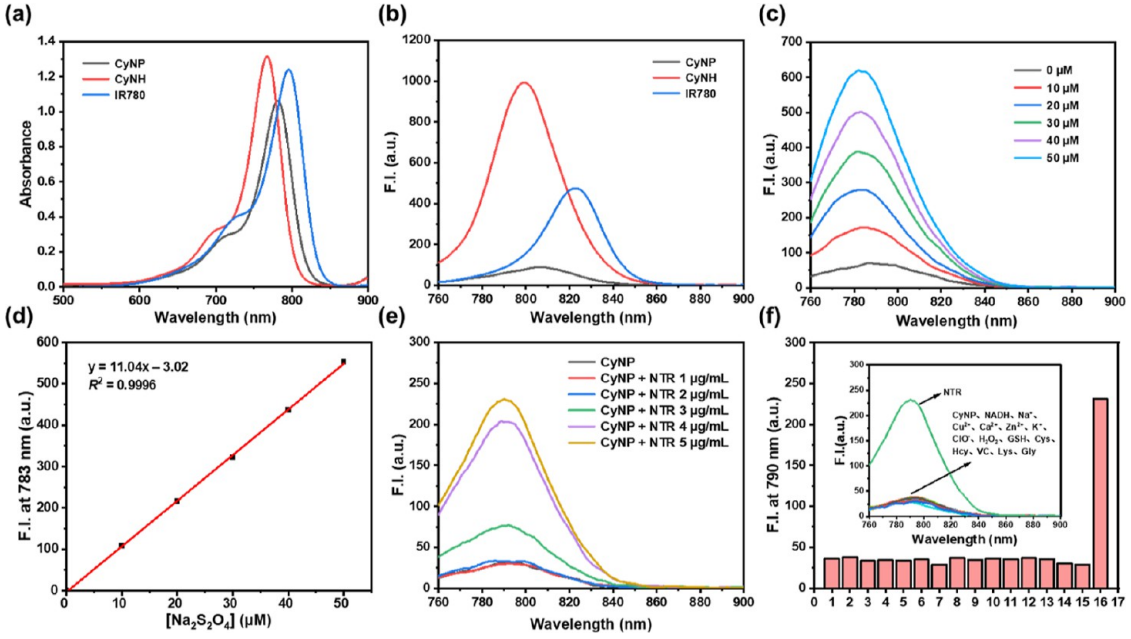

Figure 1. (a) Absorption spectra of CyNP, CyNH, and IR780 (5 μM) in DMSO. (b) Fluorescence spectra of CyNP, CyNH, and IR780 (5 μM) in DMSO. (c) Fluorescence spectra of CyNP (5 μM) interaction with $Na_2S_2O_4$. (d) Fluorescence standard curve of CyNP interaction with $Na_2S_2O_4$. (e) Fluorescence spectra of CyNP (5 μM) in response to NTR in the presence of NADH (500 μM). (f) Selectivities of 5 μM CyNP to different species: (1) only CyNP (5 μM), (2) NADH (500 μM), (3) Na^+ (10 mM), (4) Cu^{2+} (10 mM), (5) Ca^{2+} (10 mM), (6) Zn^{2+} (10 mM), (7) K^+ (10 mM), (8) ClO^- (1 mM), (9) H_2O_2 (1 mM), (10) GSH (1 mM), (11) Cys (1 mM), (12) Hcy (1 mM), (13) VC (1 mM), (14) Lys (1 mM), (15) Gly (1 mM), (16) NTR (5 μg/mL, in the presence of 500 μM NADH).

IR780 as substrate (Scheme S1), and the structures of the products were all determined by nuclear magnetic resonance (NMR) and electrospray ionization-mass spectrometry (ESI-MS) characterization (Figures S1−S6).

2.2. Photophysical Properties. As shown in Figure 1a, IR780 has a maximum absorption at 796 nm ($\varepsilon = 2.480 \times 10^5$ M^{-1} cm^{-1}), and after the introduction of the nitrobenzene group, the maximum absorption of CyNP is blue-shifted (781 nm) and the absorption coefficient is reduced ($\varepsilon = 2.126 \times 10^5$ M^{-1} cm^{-1}), and the fluorescence is substantially weaker compared to IR780 (Figure 1b) [$\Phi_{f\ (IR780)} = 15.3\%$, $\Phi_{f\ (CyNP)} = 2.3\%$]. This is due to the introduction of the nitrobenzene group, which leads to the PET effect, resulting in a weakened fluorescence. At the same time, the control molecule CyNH ($\Phi_f = 34\%$) has no PET effect and has a strong fluorescence compared to CyNP (Figure 1b).

CyNH can be obtained by reducing the nitro group of CyNP using NTR as well as sodium hydrosulfite ($Na_2S_2O_4$), a potent nitro-reducing agent. Several studies have documented the utilization of $Na_2S_2O_4$ for targeting hypoxia through its ability to reduce nitro groups.[45,46] Therefore, we first used $Na_2S_2O_4$ to verify the reduction process of CyNP. As depicted in Figure 1c, the CyNP exhibited a maximum emission wavelength of 788 nm [in phosphate-buffered saline (PBS)/DMSO = 2:1, v/v] with weak fluorescence before the reaction of CyNP with $Na_2S_2O_4$. The emission wavelength was slightly blue-shifted to 783 nm after the reaction with $Na_2S_2O_4$, suggesting that a new product might be formed. The fluorescence of the new product was enhanced with the addition of $Na_2S_2O_4$ with concentration dependence. The calculated detection limit for $Na_2S_2O_4$ using CyNP was found to be 0.18 μM, indicating its high sensitivity. The fluorescence spectra of the reduction product of CyNP with $Na_2S_2O_4$ almost overlapped with that of the synthesized amino compound CyNH (Figure S7a). To further determine the reduction mechanism of CyNP with $Na_2S_2O_4$, it was verified by high-performance liquid chromatography (HPLC) and high-resolution mass spectrometry (HRMS). The retention time of CyNP (100 μM) in the HPLC chromatogram was 3.750 min, while that of CyNH (100 μM) was 1.990 min. The reaction solution of CyNP (100 μM) and $Na_2S_2O_4$ (500 μM) appeared two peaks at 3.750 and 1.990 min, respectively, which corresponded to CyNP and CyNH (Figure S8). In addition, the reduction product of CyNP with $Na_2S_2O_4$ produced a mass peak at m/z = 596.3994 consistent with CyNH (Figure S9). Therefore, it can be inferred from the outcomes that the nitrobenzene group of CyNP was transformed into an aminophenyl group through a reduction in the presence of $Na_2S_2O_4$, resulting in the production of CyNH and fluorescence.

After conducting the verification as mentioned above, we analyzed the fluorescence changes of CyNP before and after its interaction with NTR (Figure 1e). CyNP exhibited a faint fluorescence signal, however, upon the addition of 3 μg/mL NTR, a remarkable enhancement in fluorescence intensity was observed at 790 nm, and when NTR was added to 5 μg/mL, the fluorescence was enhanced by 7.4-fold. Furthermore, the maximum emission wavelength of the reduction product of CyNP with NTR (790 nm) exhibited a slight red shift compared to that of the reduction product of CyNP with $Na_2S_2O_4$ (783 nm), which was caused by different solvent environments, the former being reacted in PBS/DMSO = 2:1 (v/v) and the latter in HEPES/DMSO = 7:3 (v/v). After the unification of the two solvent environments, their fluorescence spectra almost overlapped (Figure S7b). To study the selectivity of CyNP for NTR, the inorganic salt species (Na^+, Cu^{2+}, Ca^{2+}, Zn^{2+}, and K^+), reactive oxygen species with reducing properties (ClO^- and H_2O_2) and biological species

https://doi.org/10.1021/acsomega.4c03098
ACS Omega 2024, 9, 30685−30697

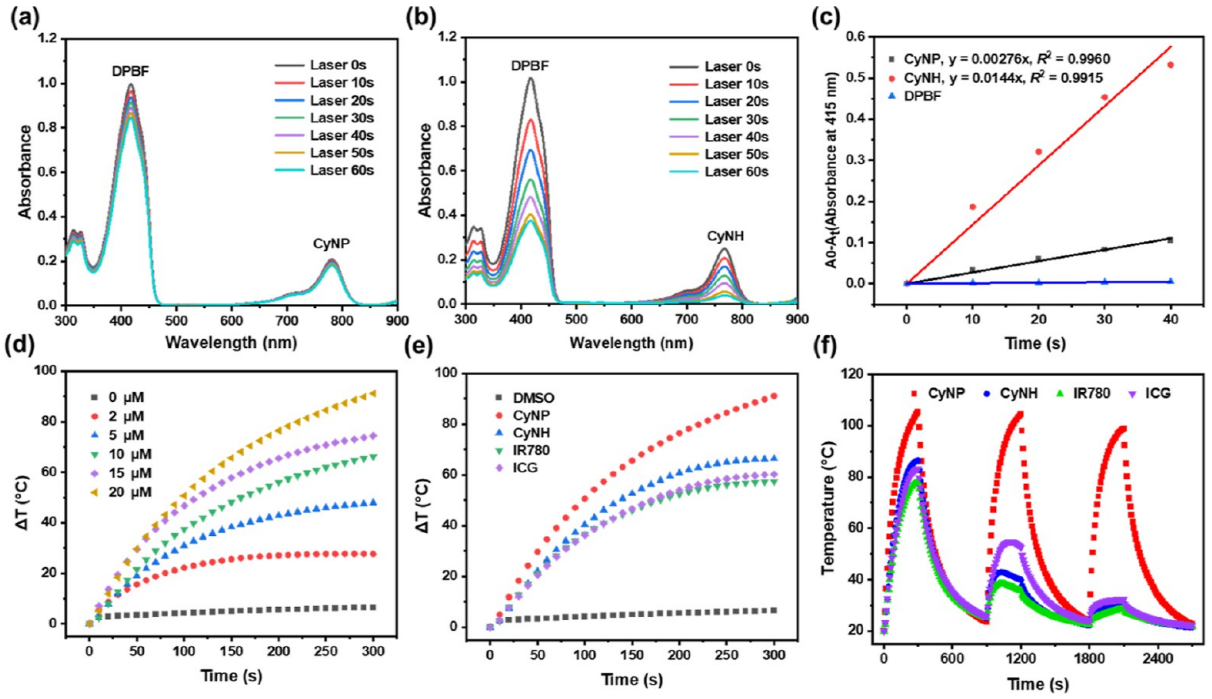

Figure 2. Absorption spectra of DPBF at 415 nm with (a) CyNP, and (b) CyNH in DMSO. (c) The linear correlation of DPBF absorbance change at 415 nm with CyNP and CyNH. (d) The photothermal temperature changes of CyNP at different concentrations (0−20 μM). (e) The photothermal temperature changes of CyNP, CyNH, IR780, and ICG (20 μM) in DMSO. (f) The photothermal stability of CyNP, CyNH, IR780, and ICG (20 μM) with three cycles (radiation for 5 min, cooling for 10 min in one cycle). 760 nm (1.5 W/cm^2) laser for all radiation.

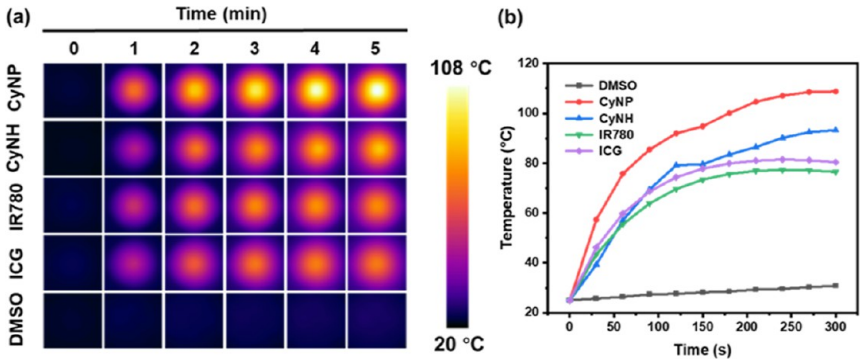

Figure 3. (a) Photothermal imaging of CyNP, CyNH, IR780, and ICG (20 μM) in DMSO under 760 nm (1.5 W/cm^2, 5 min) laser irradiation. (b) Quantification of temperature changes of (a).

[glutathione (GSH), cysteine (Cys), homocysteine (Hcy), vitamin C (Vc), lysine (Lys) glycine (Gly)] were tested and fluorescence spectra at 790 nm were recorded. Figure 1f illustrates that solely the NTR group displayed a robust fluorescence emission at 790 nm. In contrast, negligible fluorescence was observed in the remaining groups, thereby validating the exceptional specificity of CyNP toward NTR within a complex milieu.

We then used 1,3-diphenyl isobenzofuran (DPBF) to investigate the ability of CyNP and CyNH to produce $^1O_2$ under 760 nm (1.5 W/cm^2) laser irradiation. CyNP and CyNH degraded the absorption spectra of DPBF, which implied the production of $^1O_2$ (Figure 2a,b). While CyNH produced $^1O_2$ at a much higher rate than CyNP (Figure 2c), the $^1O_2$ quantum yields of CyNP (Φ_Δ = 1.4%) and CyNH (Φ_Δ = 4.7%) were calculated using ICG (Φ_Δ = 7.7% in DMSO) as the standard[14] (Figure S10). The experimental results of fluorescence and $^1O_2$ indicate that CyNP quenches its radiative leap and intersystem crossing process due to the PET effect, and when it is reduced to CyNH, the PET effect is blocked and fluorescence and $^1O_2$ are restored.

Then, we monitored the temperature changes of CyNP and CyNH in DMSO under 760 nm (1.5 W/cm^2) laser irradiation using a precision thermocouple temperature probe and thermocouple pyrometer to examine their photothermal capabilities. The composition of a solar thermal device is shown in Figure S11. We initially investigated the temperature variation of CyNP in DMSO under varying laser powers (Figure S12a) and concentrations (Figure 2d). By subjecting the CyNP solution (20 μM) to a photothermal treatment, we observed an approximate increase in temperature of 90 °C. In addition, the temperatures generated by photothermal effects were measured for CyNH, IR780, and the well-known NIR photothermal agent ICG (20 μM) under identical conditions (Figure 2e). The photothermal conversion efficiency (η) was then calculated (Figure S12b−f). Notably, the efficiency (η) of

https://doi.org/10.1021/acsomega.4c03098
ACS Omega 2024, 9, 30685−30697

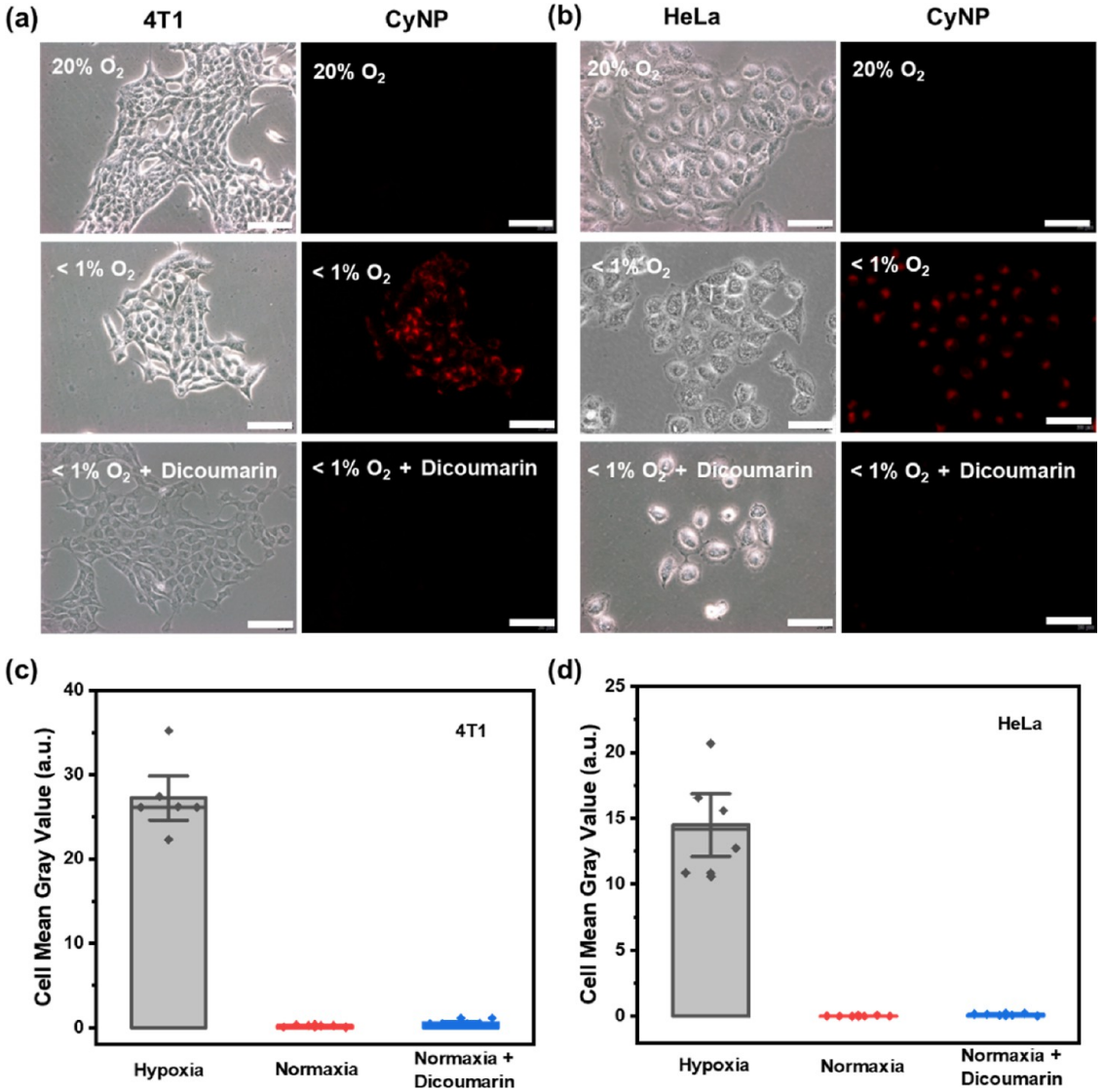

Figure 4. (a,b) Fluorescence imaging and (c,d) semiquantification of 5 μM CyNP incubated in 4T1 and HeLa cells at different oxygen concentrations. Dicoumarin (NTR inhibitor, 0.5 mM). Scale bar = 100 μm.

CyNP was found to be 21%, which is approximately twice that of IR780 (10.7%) and 1.8 times higher than that of ICG (11.7%). The efficiency (η) of CyNH is 12.9%, which is significantly weaker than CyNP. This is because the disappearance of the PET effect changes the excited state deactivation pathway of CyNH, and the radiative leap and intersystem crossing pathways originally inhibited by the PET effect are restored to compete for energy with the nonradiative leap photothermal pathway.

According to the test results of these optical properties, CyNP exhibits high photothermal conversion efficiency with excellent photothermal performance. At the same time, CyNH is similar to IR780 and ICG, in that the radiative and nonradiative leap processes compete with each other for energy and exhibit high fluorescence quantum yields, single-linear state oxygen yields, and photothermal conversion efficiency. All the optical parameters that underwent testing have been consolidated and presented in Table S1. To examine the photothermal stability of these PSs, we recorded the temperature change of these PSs over time through three "radiation-cooling" photothermal cycles. As shown in Figure 2f, the highest temperature of CyNP reached the same level in all three photothermal cycles. At the same time, CyNH, IR780, and ICG were already degraded in the second cycle, suggesting that CyNP has better photothermal stability, which may be related to the PET effect affecting its electron transfer and energy transfer pathways, which inhibits its photolysis reaction to some extent. In addition, the temperature variations induced by photothermal effects in these PSs were observed using a photothermal imager (Figure 3a,b), and the imaging outcomes demonstrated agreement with the aforementioned findings.

2.3. In Vitro Application. The expression of NTR in tumor cells is directly correlated with the level of cellular hypoxia.[47] Therefore, we induced overexpression of NTR in cells by creating a hypoxic environment and investigated CyNP's ability to detect NTR in hypoxic cells. First, we validated the expression of NTR in hypoxic cells using the ROS-ID Hypoxia/Oxidative Stress Detection Kit (Figure S13). The hypoxia red detection reagent (probe) in the kit is a nonfluorescent or weakly fluorescent nitroaromatic compound. It can react with NTR to convert nitro groups into hydroxylamine (NHOH) and amino groups (NH_2) through

https://doi.org/10.1021/acsomega.4c03098
ACS Omega 2024, 9, 30685−30697

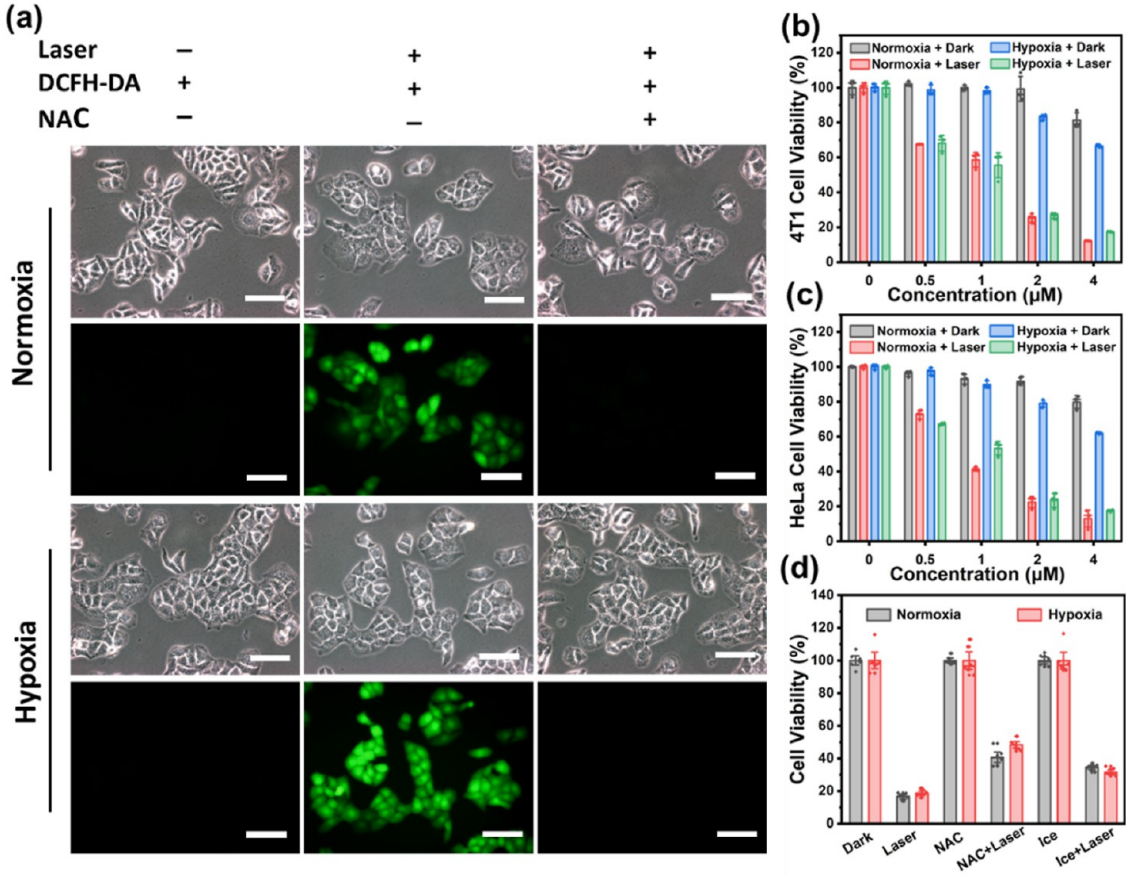

Figure 5. (a) DCFH-DA (5 μM) assesses ROS levels of CyNP (5 μM) in HeLa cells intrinsically irradiated with a 760 nm (1.5 W/cm^2, 3 min) laser. NAC was 5 mM. Scale bar = 100 μm. (b,c) 4T1 and HeLa cells viability treated with 0−4 μM CyNP (n = 3, mean ± 1.5 SD). (d) 4T1 cells viability treated with CyNP (2 μM) under different conditions (n = 6, mean ± 1.5 SD). Conditions: A laser using 760 nm (1.5 W/cm^2) radiation 5 min. The NAC concentration was 10 mM and incubated for 1 h at the end of the hypoxia. To provide an ice bath by adjusting the water temperature to 4−10 °C with ice packs. Normoxia: 20% O_2, and hypoxia: < 1% O_2.

a series of chemical reactions and release fluorescence, which is used for the detection of cell hypoxia level.[48] HeLa cells and 4T1 cells were chosen for preincubation in both normal oxygen levels (20% O_2) and hypoxic conditions (<1% O_2) (hypoxic condition was created by passing 95% N_2 + 5% CO_2 through hypoxic chambers) for 8 h,[30] they were incubated with hypoxia red detection reagent (1 μM) for 30 min. Meanwhile, dicoumarin (an NTR inhibitor) was used as a control for the hypoxic group, where hypoxic cells were incubated with dicoumarin (0.5 mM) for 1 h to inhibit the expression of NTR, followed by incubation with the hypoxia red detection reagent (probe) for 30 min, and then imaged under the same fluorescence conditions. This probe showed weak fluorescence in normoxic cells, but emited strong red fluorescence in hypoxic cells. The fluorescence disappeared upon addition of an NTR inhibitor (Figure S13). These observations indicate the induction of NTR in the hypoxic cellular environment.

Based on this, the detection performance of CyNP in hypoxic cells for NTR was examined using the same experimental procedures. CyNP (5 μM) was incubated for 4 h in normoxic and hypoxic cells, and no significant fluorescence signal was detected in the normoxic cells, while a clear red fluorescence was observed in the hypoxic cells (Figure 4). After pretreatment with NTR inhibitors, the red fluorescence of CyNP disappeared in the hypoxic cells (Figure 4). The statistical analysis of the intensity of cell fluorescence imaging (Figure 4c,d) corroborated these findings. These results were consistent with the results of the commercial NTR probe (hypoxia red detection reagent), indicating that CyNP can detect NTR in hypoxic cells and can be used for hypoxic cell imaging.

2,7-dichlorofluorescein diacetate (DCFH-DA) was utilized to assess the production of ROS in HeLa cells treated with CyNP under both normal oxygen levels (20% O_2) and low oxygen levels (<1% O_2). Figure 5a demonstrates that cells exposed to a 760 nm laser exhibited green fluorescence, indicating the generation of ROS by CyNP within the cells. However, when *N*-acetyl-*L*-cysteine (NAC), a scavenger for ROS,[49] was added to the cells, the green fluorescence signal disappeared upon exposure to the 760 nm laser radiation. These findings were consistent regardless of whether the cells were subjected to normal or low oxygen conditions.

Furthermore, using CCK-8 assay to evaluate cell viability, 4T1 and HeLa cells were exposed to various conditions and compared with CyNH as a control to investigate the in vitro phototherapeutic properties of CyNP. To begin with, we examined the impact of varying concentrations of CyNP and CyNH on the two cells under normoxic and hypoxic conditions using laser radiation at 760 nm (1.5 W/cm^2, 5 min). The phototoxicity IC_{50} values have been compiled and presented in Table S2. In contrast, CyNH showed better cell phototoxicity in hypoxic conditions (Figure S14 and Table S2), implying that CyNP fully converted into CyNH in hypoxic state may have better in vitro tumor cell therapeutic

https://doi.org/10.1021/acsomega.4c03098
ACS Omega 2024, 9, 30685−30697

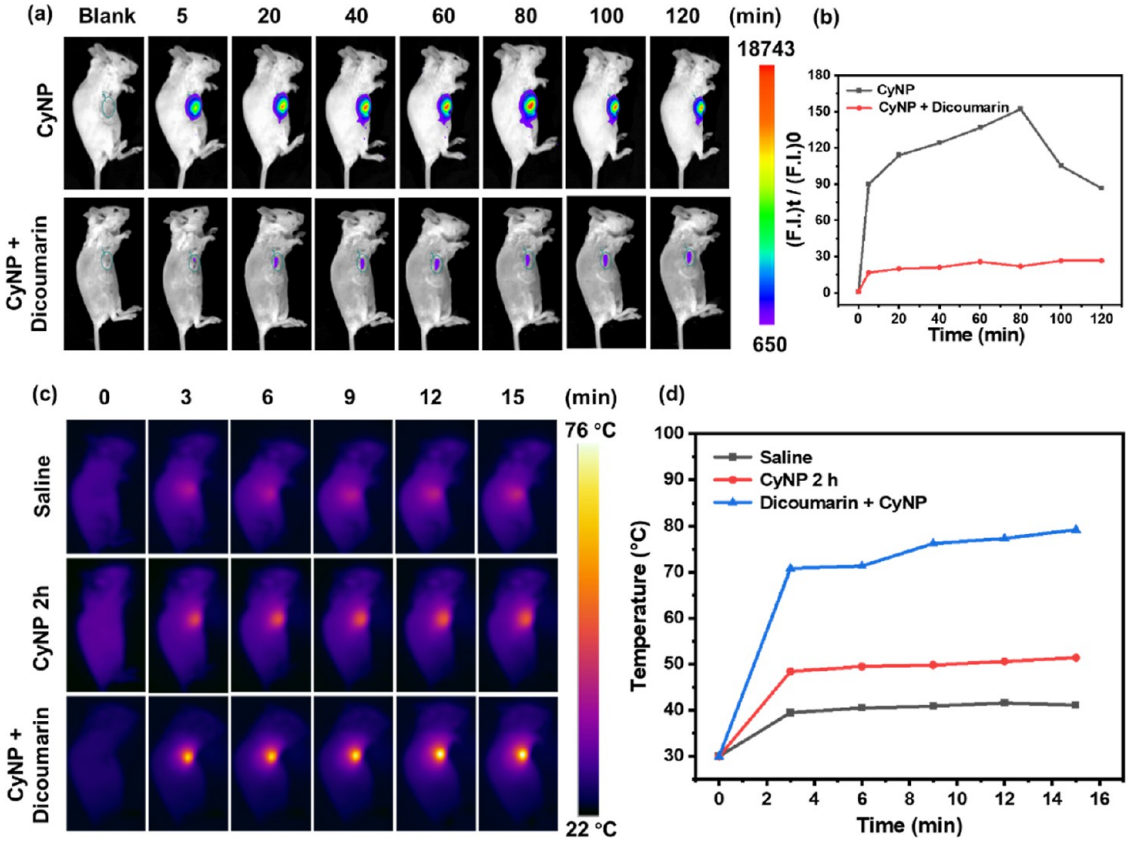

Figure 6. (a) Fluorescence imaging and (b) fluorescence intensities quantization of the 4T1 tumor model with intratumor injections of CyNP (200 μM) and CyNP (200 μM) + dicoumarin (1 mM) (n = 3). (c) Photothermal imaging and (d) temperature of the 4T1 tumor model after intratumorally injecting with saline, CyNP (200 μM), and CyNP (200 μM) + dicoumarin (1 mM) under 760 nm (1.5 W/cm^2, 15 min) laser irradiation (n = 3).

effects. However, CyNP showed better cell phototoxicity than in hypoxic conditions in normoxic conditions (Figure 5b,c and Table S2), which may be because CyNP did not fully convert into CyNH in this hypoxic environment. However, both CyNP and CyNH showed good cell phototoxicity, suggesting that CyNP may be able to exert good tumor therapeutic effects in both normoxic and hypoxic regions of tumors. To investigate the phototherapeutic performance of PTT or PDT before and after the reduction of CyNP under normoxic and hypoxic conditions. NAC was used to remove intracellular ROS to examine the PTT performance alone or to keep the cells at low temperatures during radiation by an ice bath to examine the PDT performance alone.[14] The results are shown in Figure 5d. Cells treated with CyNP exhibited a notable decrease in cell viability when exposed to radiation, suggesting that both CyNP and its reduced form, CyNH, demonstrated enhanced phototherapeutic effects on the processes of PTT or PDT.

2.4. In Vivo Application. To assess the in vivo response of CyNP to NTR, we created a tumor model in BALB/c mice bearing 4T1 tumors and examined the fluorescence imaging of CyNP at the site of the tumor through the administration of both CyNP and dicoumarin.[14,39,40] As shown in Figure 6a,b, on the one hand, after CyNP (200 μM) was injected into the tumor site, fluorescence was responded to at 5 min, and the fluorescence intensity reached the strongest at 80 min, which was 150 times that before the response. On the other hand, intratumoral injection of dicoumarin (1 mM) for 30 min to inhibit NTR expression was followed by CyNP (200 μM), at which time no significant fluorescence signal was observed. The results demonstrate that within the tumor, NTR selectively activates CyNP fluorescence, suggesting that CyNP can be utilized for real-time detection of hypoxic tumors.

Furthermore, the photothermal therapeutic efficacy of each treatment group within the tumor was evaluated by monitoring temperature fluctuations at the tumor site using 760 nm (1.5 W/cm^2) laser radiation (Figure 6c,d). On the one hand, to maximize the monitoring of the photothermal temperature of CyNP within the tumor, NTR inhibitors were preinjected to interact with the tumor for 30 min before CyNP was given and immediately radiated and imaged. On the other hand, to monitor the photothermal temperature of CyNP after it was reduced within the tumor, radiation and photothermal imaging were performed 2 h after intratumoral injection of CyNP according to the fluorescence imaging results. Meanwhile, saline was used as a control. The temperature of the group injected with NTR inhibitor and CyNP was 35 °C higher than that of the saline group, while the final temperature of the group injected with CyNP for 2 h also reached 51 °C, which could effectively ablate the tumor.

Finally, we examined the in vivo tumor phototherapy effect of CyNP guided by fluorescence imaging and photothermal imaging. Treatment by intratumoral injection of CyNP as well as saline was used to compare the effect of tumor treatment for 7 days (Figure 7a–d). The mice with tumors were divided into 4 groups in a random manner and subjected to treatments including "Saline", "Saline + Laser", "CyNP", and "CyNP + Laser". To ensure the simultaneous presence of CyNP and

https://doi.org/10.1021/acsomega.4c03098
ACS Omega 2024, 9, 30685−30697

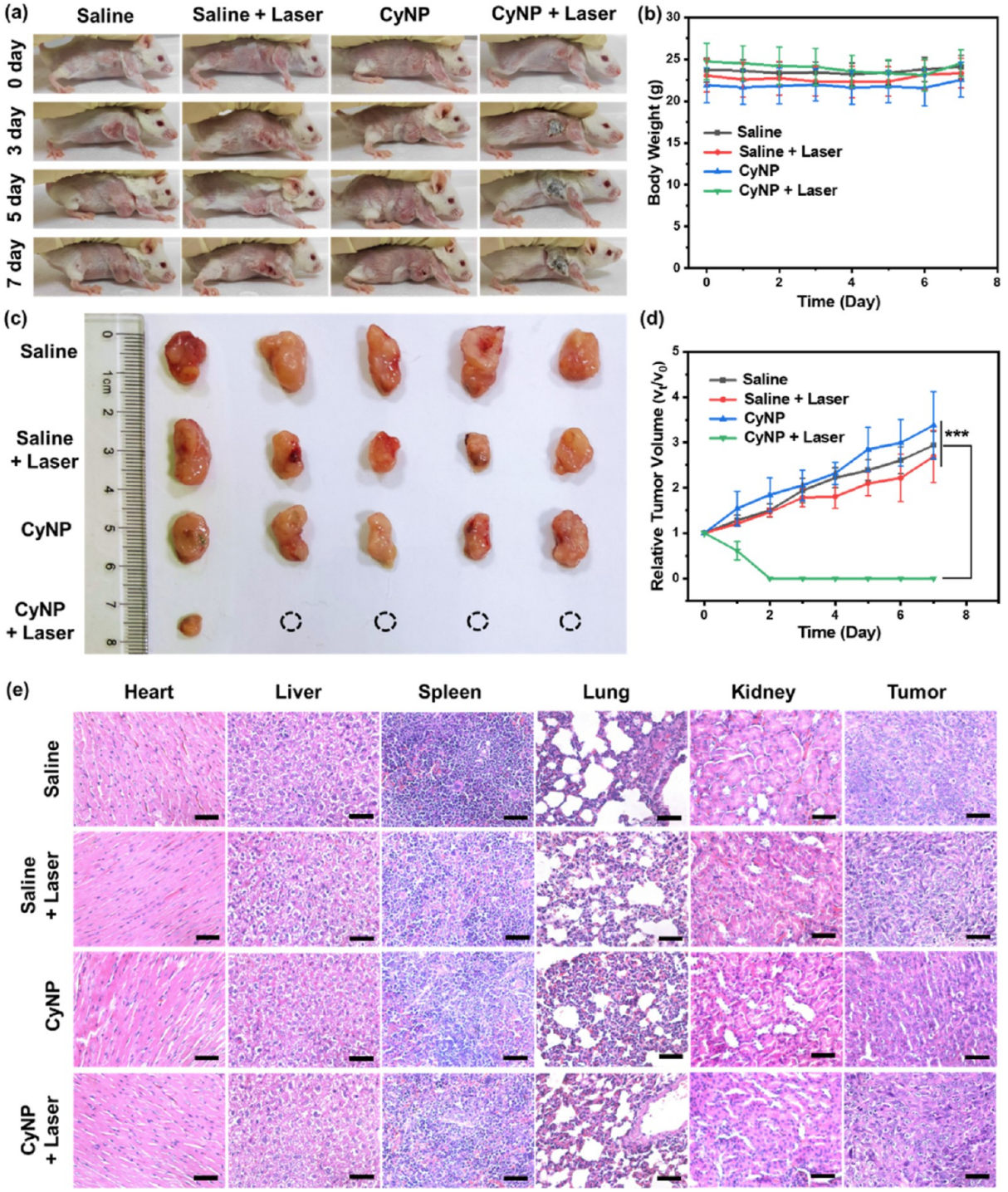

Figure 7. (a) Photographs of 4T1 tumor model after 7 days of phototherapy in each group (760 nm, 1.5 W/cm^2, 15 min). (b) Body weights of the mice after different treatments within 7 days (n = 5, mean ± SD). (c) Images of tumors harvested from the mice after different treatments within 7 days. (d) Relative tumor volume of the mice after different treatments within 7 days (n = 5, mean ± SD). Two-tailed Student's t-test was used for statistical analysis, ***P < 0.001. (e) H&E staining of the major organs and tumor tissues from different treatment groups after 7 days of treatment (Scale bar = 50 μm) (n = 5).

CyNH in the tumor, according to the fluorescence imaging results, the fluorescence intensity reached half of the maximum value within 5 min after injection, when CyNP was not completely reduced to CyNH. Therefore, the tumor was irradiated with a laser (760 nm, 1.5 W/cm^2) for 15 min at this time. After two consecutive days of treatment, the tumor was completely ablated in the "CyNP + Laser" group (Figure 7d), and only one case of metastatic recurrence was found in the next 5 days without injection and irradiation treatment (Figure 7c), while the other three groups were treated in parallel. After 7 days of treatment, the "Saline", "Saline + Laser", and "CyNP" groups did not show tumor suppression, and their tumor volumes continued to grow (Figure 7d), while the "CyNP + Laser" group showed good tumor therapeutic effects. The photographs of the mice during treatment (Figure 7a) and the isolated tumors on the seventh day of treatment (Figure 7c)

https://doi.org/10.1021/acsomega.4c03098
ACS Omega 2024, 9, 30685−30697

further supported this result. The serum biochemical markers (Figure S15) and histopathological analysis using hematoxylin and eosin staining (H&E) (Figure 7e) of major organs, including the heart, liver, spleen, lung, and kidney, as well as tumor tissues in mice after treatment completion revealed that CyNP exhibited minimal toxicity in vivo. There were no evident signs of organ damage or lesions observed, and the body weight of mice remained stable throughout the treatment period. These findings suggest that CyNP demonstrates favorable biocompatibility for in vivo tumor therapy.

3. CONCLUSIONS

In summary, we designed and synthesized an intelligent and efficient novel PS (CyNP) for tumor fluorescence imaging and therapy. The preparation of CyNP is simple and readily available, and it cleverly takes advantage of the physiological characteristics of tumor hypoxia to achieve NIR fluorescence imaging of hypoxic tumors and a highly efficient tumor treatment through the synergy of PTT and PDT. CyNP changes its chemical structure in the presence of $Na_2S_2O_4$ or NTR by reducing from a nitrobenzene group to an aminophenyl group (CyNH), this transition allows the nitro-mediated PET effect to be blocked and its excited state deactivation pathway to be altered. This means that CyNP, which exerts PTT properties, and CyNH, which has PDT and PTT properties, are contained in solid tumors, and that the reduction of CyNP to CyNH turns on NIR fluorescence, which is of guiding importance for real-time imaging and treatment of hypoxic tumors. This strategy was validated by both molecular spectroscopy and in vitro tumor cell experiments. In addition, CyNP applied to in vivo tumor treatment in mice showed a surprisingly efficient therapeutic effect with complete tumor ablation on the second day of treatment and a low tumor recurrence rate within a short period. This flexible strategy we propose achieves effective treatment of tumors in a simple yet efficient manner. It provides a reference for the design ideas of smart PS.

4. MATERIALS AND METHODS

4.1. Materials and Instruments. The chemicals utilized in the study were procured from Energy Chemical Co. Ltd. (China) and J&K Scientific Co. Ltd. (China), while all solvents employed were of analytical grade. The NTR powder was acquired from Sigma-Aldrich, while the NADH was obtained from J&K Scientific Co. Ltd., a Chinese supplier. The NMR spectra were observed using an Agilent 400 DD2 spectrometer (^{1}H NMR, 400 MHz; ^{13}C NMR, 100 MHz) from Agilent in Palo Alto, USA. Mass spectrometry data (ESI-MS) were acquired utilizing a Time-of-flight Micromass LCT Premier XE Spectrometer manufactured by McKinley in NJ, USA, and Aglient6550qtof & Thermo Fisher-QE instruments. The UV-2600i UV−vis spectrophotometer (manufactured by Shimadzu Instruments Co., Ltd. in Suzhou, China) was utilized to acquire absorption spectra, while the Carry Eclipse fluorescence spectrophotometer (provided by Agilent Technologies Co., Ltd. in China) was employed for obtaining fluorescence spectra. Conduct experiments to verify the reduction mechanism using an Agilent 1260 liquid chromatograph (manufactured by Agilent, USA). The 760 nm NIR laser was acquired from a Chinese company called Changchun Femtosecond Technology Co. Ltd. Photothermal temperature testing is achieved with a K-type armor thermocouple (KAIPUSEN Temperature sensor, KPS-IN600-K1.0-SMPW-K-M, 0.5 mm × 150 mm) and a thermocouple temperature logger (YET-610). Photothermal imaging experiments were performed utilizing a thermal imaging camera (Fotric 225s#L24, A company of ZXF Laboratories, LLC). The 4T1 and HeLa cells were from KeyGen BioTech Co., Ltd. (Jiangsu, China). The cellular hypoxic environment was provided by a hypoxia chamber (Stemcell Technologies, Cat 27310, US) supplied with a gas mixture (95% N_2 + 5% CO_2). NTR detection in cells was performed using ROS-ID Hypoxia/Oxidative Stress Detection Kit (ENZ-51042-0125, Enzo life science, USA). Fluorescence imaging of cells was conducted using an inverted microscope, specifically the Olympus IX73 + DP73 model. For animal fluorescence imaging, we utilized the NightOWL II LB983 small animal imaging system (Berthold Technologies Gmbh & Co. KG).

4.2. Synthesis of CyNP. IR780 (100 mg, 1 equiv), 4-nitrophenylboronic acid (75 mg, 3 equiv), $Pd(OAc)_2$ (10 mg, 30%), X-Phos (43 mg, 60%), and Cs_2CO_3 (49 mg, 1 equiv) were weighed in two flasks and 10 mL of EtOH and tetrabutylammonium fluoride (1 M in THF) (450 μL, 3 equiv) were added under nitrogen protection and stirred at reflux in an oil bath for 6 h. At the end of the reaction, the green constituent was isolated through separation using 200−300 mesh silica gel and eluted with a mixture of MeOH/DCM in a ratio of 1:20 (v/v). This resulted in the formation of a solid green product weighing 60 mg, with a yield of 53%. ^{1}H NMR (400 MHz, DMSO-d_6): δ 8.53 (d, J = 8.4 Hz, 2H), 7.62 (d, J = 8.4 Hz, 2H), 7.48 (d, J = 7.4 Hz, 2H), 7.36 (d, J = 6.5 Hz, 4H), 7.18 (t, J = 6.9 Hz, 2H), 6.91 (d, J = 14.0 Hz, 2H), 6.27 (d, J = 14.0 Hz, 2H), 4.12 (t, J = 5.6 Hz, 4H), 2.71 (t, J = 5.1 Hz, 4H), 2.01−1.93 (m, 2H), 1.72 (dd, J = 14.4, 7.2 Hz, 4H), 1.11 (s, 12H), 0.92 (t, J = 7.3 Hz, 6H). ^{13}C NMR (100 MHz, DMSO-d_6): δ 171.9, 158.2, 147.4, 146.9, 146.6, 142.5, 141.0, 131.5, 130.7, 128.8, 125.2, 124.1, 122.8, 111.6, 100.9, 48.7, 45.2, 28.1, 27.4, 24.5, 20.8, 11.5; HRMS (ESI-MS) ($C_{42}H_{48}N_3O_2^+$) m/z: $[M]^+$ calcd 626.3742; found, 626.3675.

4.3. Synthesis of CyNH. IR780 (100 mg, 1 equiv), 4-aminophenyl boronic acid hydrochloride (78 mg, 3 equiv), $Pd(OAc)_2$ (10 mg, 30%), X-Phos (43 mg, 60%), Cs_2CO_3 (49 mg, 1 equiv) were weighed in a two-necked flask and 10 mL of EtOH and tetrabutylammonium fluoride (1 M in THF) (450 μL, 3 equiv) were added under nitrogen protection and refluxed in an oil bath with stirring for 6 h. After the reaction, a green compound was isolated through separation using 200−300 mesh silica gel and eluted with a mixture of MeOH/DCM in a ratio of 1:20 (v/v). This process yielded a solid green product weighing 70 mg, with an overall yield of 61%. ^{1}H NMR (400 MHz, DMSO-d_6): δ 7.50 (d, J = 7.4 Hz, 2H), 7.42−7.33 (m, 6H), 7.16 (t, J = 7.9 Hz, 2H), 6.86 (d, J = 8.2 Hz, 2H), 6.77 (d, J = 8.2 Hz, 2H), 6.19 (d, J = 14.2 Hz, 2H), 5.48 (s, 2H), 4.09 (t, J = 6.9 Hz, 4H), 2.65 (t, J = 5.5 Hz, 4H), 1.95−1.86 (m, 2H), 1.71 (dt, J = 14.3, 7.1 Hz, 4H), 1.24 (s, 12H), 0.93 (t, J = 7.3 Hz, 6H). ^{13}C NMR (100 MHz, DMSO-d_6): δ 171.4, 164.0, 149.3, 147.8, 142.8, 140.9, 131.5, 130.7, 128.8, 124.8, 122.8, 113.7, 111.2, 100.1, 48.6, 45.0, 27.7, 24.7, 21.4, 20.7, 11.6. HRMS (ESI-MS) ($C_{42}H_{50}N_3^+$) m/z: $[M]^+$ calcd 596.3999; found, 596.3994.

4.4. Absorption and Fluorescence Spectroscopy. PSs were prepared as a stock solution of DMSO (1 mM). The measurements of the absorption and fluorescence spectra for CyNP, CyNH, and IR780 (5 μM) were conducted in DMSO. The fluorescence response spectra of CyNP with $Na_2S_2O_4$

https://doi.org/10.1021/acsomega.4c03098
ACS Omega 2024, 9, 30685−30697

were measured in a solvent mixture of PBS (10 mM, pH = 7.4) and DMSO (PBS/DMSO = 2:1, v/v). The response of CyNP to NTR was measured in a solvent mixture of HEPES buffer solution (10 mM, pH = 7.4) and DMSO (HEPES/DMSO = 7:3, v/v). NTR was prepared in pure water as an aqueous solution of 100 μg/mL per tube and stored frozen at −20 °C. CyNP to NTR selectivity assays were performed on 10 mM of various ions: Na^+, Cu^{2+}, Ca^{2+}, Zn^{2+}, K^+ and 1 mM of various substances: ClO^-, H_2O_2, GSH, Cys, Hcy, VC, Lys, Gly, and NTR (5 μg/mL).

4.5. Reduction Mechanism of CyNP. The column used was Agilent Extend C18 (150 mm × 4.6 mm, 3.5 μm), and the mobile phase consisted of 0.1% TFA solution (A) and acetonitrile (B). Gradient elution was used (0−10 min, 20% A, 80% B), with a detection wavelength of 280 nm, a flow rate of 1.0 mL·min^{-1}, a column temperature of 37 °C, and an injection volume of 10 μL. CyNP and CyNH were dissolved in methanol for chromatography, and a solution of CyNP (100 μM) and $Na_2S_2O_4$ (500 μM) with methanol/water = 1:1 (v/v) was prepared . All samples were filtered through a 0.22 μm filter. Subsequently, HRMS analysis was performed on the CyNP and $Na_2S_2O_4$ solution. The Supporting Information contains the spectral data for reference (Figures S8 and S9).

4.6. Cellular Fluorescence Imaging. To begin with, 4T1 and HeLa cells were trypsinized and cultured in Petri dishes for 24 h under normal conditions (20% O_2), and then, these cells were subjected to normoxic or hypoxic environments for another 8 h. Next, these cells were exposed to hypoxia red detection reagent (1 μM) for 30 min or CyNP (5 μM) for 4 h, while the another hypoxic group was preincubated with dicoumarin (0.5 mM) for 1 h, followed by probes. Subsequently, the cells underwent a thorough washing process using PBS solution and fresh medium was added. The imaging procedure was promptly conducted using an inverted fluorescence microscopy system manufactured by Olympus IX73. The fluorescence intensity of the cells was assessed using ImageJ software. Randomly selected areas, consisting of six cell regions and three background regions, were circled within the image utilizing ImageJ software. The mean gray value (Mean) of the circled cells was then determined. Subsequently, the average Mean values of both the six cells and three backgrounds were calculated separately. Finally, by subtracting the average Mean value obtained from the background regions from that obtained from the cell regions, we derived an average fluorescence intensity measurement for this group.

4.7. Cellular ROS Fluorescence Imaging. Under normal conditions, 4T1 and HeLa cells were inoculated and cultured in Petri dishes for 24 h. Subsequently, the cells were incubated in a normoxic or hypoxic environment for an additional 8 h. Subsequently, CyNP (5 μM) was added and incubation was continued for 4 h under normoxic or hypoxic conditions, respectively. After replacing the fresh medium and adding DCFH-DA (5 μM) for 30 min of incubation, the samples were immediately imaged using an inverted fluorescence microscope (Olympus IX73) with or without exposure to laser radiation (760 nm, 1.5 W/cm^2 for 3 min). In addition, NAC was used as a scavenger of ROS. After CyNP incubation, cells were treated with NAC (5 mM) for 1 h. ROS production was then monitored using DCFH-DA. The procedure involved washing the cells with PBS each time the medium was changed while keeping all other steps intact. Throughout the experiment, cells in the hypoxic group were subjected to anoxic conditions with reagents.

4.8. In Vitro Photothermal and Photodynamic Therapy. To study the effect of CyNP on photothermal or photodynamic treatment of 4T1 cells under a normoxic or hypoxic environment. To begin with, 4T1 cells were inoculated in 96-well plates and cultured under normal conditions for 24 h. Then, the cells were incubated under normal or low oxygen levels for an additional 8 h. Afterward, CyNP (2 μM) was added and incubated for an additional 4 h in normoxia or hypoxia, respectively. The temperature generated by the photothermal treatment was lowered using an ice−water bath to examine the photodynamic effect alone, and the NAC was used to scavenge the generated ROS to inhibit the photodynamic treatment, and to examine the cell-killing effect of the photothermal treatment only. The "ice + laser" group was irradiated in an ice bath with an ice pack to adjust the water temperature to 4−10 °C; the "NAC + laser" group was pretreated with NAC (10 mM) for 1 h before CyNP administration, and then irradiated after 4 h of incubation with CyNP. The incubation was continued for 24 h after the end of the irradiation, and the cell viability of all groups was detected by CCK-8.

4.9. Animal Feeding and Tumor Modeling. All animal studies were carried out in strict compliance with the Guide for the Care and Use of Laboratory Animals and were approved by the Ethics Committee of Zunyi Medical University. Female BALB/c mice (6−8 weeks, 18−22 g, n = 50) were obtained from the Experimental Animal Center of Zunyi Medical University [SPF class, production license number: SCXK-(Qian)2021-0002, use license number: SCXK(Qian)2021-0004]. All experimental animals were housed in separate cages (n = 5−6 animals/cage), maintained with good ventilation, constant temperature (23 ± 1 °C), constant humidity (55 ± 5%), 12 h day/night alternation, and all animals were fed with standard laboratory chow. No animals died during the experimental process.

Tumor model establishment: Mice were depilated and 100 μL of 4T1 cells were injected into the mammary fat pads in the axilla at a concentration of 1.5 × 10^7 cells/mL. mice were reared as normal, and experiments were carried out when the tumors had reached a volume of 150 mm^3.[40,50] All CyNP injections consisted of a 200 μM solution in pH 7.4 HEPES containing 10% DMSO.

4.10. In Vivo Fluorescence and Photothermal Imaging. To examine the effect of CyNP on NTR within solid tumors, NTR was inhibited by intratumoral injection of 50 μL of dicoumarin (1 mM, 30 min), followed by CyNP (200 μM, 50 μL), and compared with that of ruffed mice injected with CyNP only. Fluorescence imaging was performed using a small animal imaging system (λ_{ex} = 740 nm ± 20 nm, λ_{em} = 800 nm ± 20 nm).

To monitor the photothermal temperature profile of CyNP action in tumors, the "saline group", "CyNP group" and "CyNP + dicoumarin group" were set up for examination. Saline (50 μL) and CyNP (200 μM, 50 μL) were injected intratumorally for 2 h, and then the tumor was irradiated with laser (760 nm, 1.5 W/cm^2, 15 min), and the temperature of the tumor was monitored by a photothermal imaging camera. To prevent CyNP from being reduced to CyNH by the NTR in the tumor, the "CyNP + dicoumarin group" was preinjected with dicoumarin (1 mM) for 30 min, and then irradiated and imaged after treated with CyNP (200 μM, 50 μL) for 5 min.

4.11. In Vivo Tumor Phototherapy of Mice. Four groups were formed by randomly assigning BALB/c mice with

https://doi.org/10.1021/acsomega.4c03098
ACS Omega 2024, 9, 30685−30697

tumors (n = 5): the "saline" group, the "saline + laser" group, the "CyNP" group, and the "CyNP + laser" group. The "saline" group and the "CyNP" group were injected intratumorally saline (50 μL) and CyNP (200 μM, 50 μL) respectively. After a 5 min administration of these substances, the tumor site was exposed to laser irradiation (760 nm, 1.5 W/cm^2) for 15 min. The treatment period was 7 days, with no further treatment or radiation for the remaining 5 days after two consecutive days of injection and radiation. The mice were subjected to daily weighing, while the measurement and documentation of tumor volumes were conducted daily. Following 7 days, H&E staining techniques were employed for examining the tumor tissues in mice.

■ ASSOCIATED CONTENT

Supporting Information

The Supporting Information is available free of charge at https://pubs.acs.org/doi/10.1021/acsomega.4c03098.

Additional data, including ^{1}H NMR, ^{13}C NMR, ESI-Mass, optical property tests (fluorescence quantum yield, singlet oxygen quantum yield, and photothermal conversion efficiency), cell culture and toxicity assessment, and biocompatibility assessment (PDF)

■ AUTHOR INFORMATION

Corresponding Authors

Jie Gao − *College of Pharmacy, Zunyi Medical University, Zunyi, Guizhou 563003, China; Guizhou International Scientific and Technological Cooperation Base for Medical Photo−Theranostics Technology and Innovative Drug Development, Zunyi, Guizhou 563003, China; Key Laboratory of Basic Pharmacology of Ministry of Education and Joint International Research Laboratory of Ethnomedicine of Ministry of Education, Zunyi Medical University, Zunyi, Guizhou 563000, China;* orcid.org/0000-0002-6143-6284; Email: jiegao@mail.nankai.edu.cn

Zeli Yuan − *College of Pharmacy, Zunyi Medical University, Zunyi, Guizhou 563003, China; Guizhou International Scientific and Technological Cooperation Base for Medical Photo−Theranostics Technology and Innovative Drug Development, Zunyi, Guizhou 563003, China; Key Laboratory of Basic Pharmacology of Ministry of Education and Joint International Research Laboratory of Ethnomedicine of Ministry of Education, Zunyi Medical University, Zunyi, Guizhou 563000, China;* orcid.org/0000-0001-5354-769X; Email: zlyuan@zmu.edu.cn

Authors

Dan Shen − *College of Pharmacy, Zunyi Medical University, Zunyi, Guizhou 563003, China; Guizhou International Scientific and Technological Cooperation Base for Medical Photo−Theranostics Technology and Innovative Drug Development, Zunyi, Guizhou 563003, China; Key Laboratory of Basic Pharmacology of Ministry of Education and Joint International Research Laboratory of Ethnomedicine of Ministry of Education, Zunyi Medical University, Zunyi, Guizhou 563000, China*

Shangli Ding − *College of Pharmacy, Zunyi Medical University, Zunyi, Guizhou 563003, China; Guizhou International Scientific and Technological Cooperation Base for Medical Photo−Theranostics Technology and Innovative Drug Development, Zunyi, Guizhou 563003, China; Key Laboratory of Basic Pharmacology of Ministry of Education and Joint International Research Laboratory of Ethnomedicine of Ministry of Education, Zunyi Medical University, Zunyi, Guizhou 563000, China*

Quan Lu − *College of Pharmacy, Zunyi Medical University, Zunyi, Guizhou 563003, China; Guizhou International Scientific and Technological Cooperation Base for Medical Photo−Theranostics Technology and Innovative Drug Development, Zunyi, Guizhou 563003, China; Key Laboratory of Basic Pharmacology of Ministry of Education and Joint International Research Laboratory of Ethnomedicine of Ministry of Education, Zunyi Medical University, Zunyi, Guizhou 563000, China*

Zhengjun Chen − *College of Pharmacy, Zunyi Medical University, Zunyi, Guizhou 563003, China; Guizhou International Scientific and Technological Cooperation Base for Medical Photo−Theranostics Technology and Innovative Drug Development, Zunyi, Guizhou 563003, China; Key Laboratory of Basic Pharmacology of Ministry of Education and Joint International Research Laboratory of Ethnomedicine of Ministry of Education, Zunyi Medical University, Zunyi, Guizhou 563000, China*

Ling Chen − *College of Pharmacy, Zunyi Medical University, Zunyi, Guizhou 563003, China; Guizhou International Scientific and Technological Cooperation Base for Medical Photo−Theranostics Technology and Innovative Drug Development, Zunyi, Guizhou 563003, China; Key Laboratory of Basic Pharmacology of Ministry of Education and Joint International Research Laboratory of Ethnomedicine of Ministry of Education, Zunyi Medical University, Zunyi, Guizhou 563000, China*

Jiajia Lv − *College of Pharmacy, Zunyi Medical University, Zunyi, Guizhou 563003, China; Guizhou International Scientific and Technological Cooperation Base for Medical Photo−Theranostics Technology and Innovative Drug Development, Zunyi, Guizhou 563003, China; Key Laboratory of Basic Pharmacology of Ministry of Education and Joint International Research Laboratory of Ethnomedicine of Ministry of Education, Zunyi Medical University, Zunyi, Guizhou 563000, China*

Complete contact information is available at: https://pubs.acs.org/10.1021/acsomega.4c03098

Author Contributions

‖These authors contributed equally to this work.

Notes

The authors declare no competing financial interest.

■ ACKNOWLEDGMENTS

We are grateful for the financial support from the Natural Science Foundation of China (Grant no. 82060626, 81360471), Guizhou Science and Technology Support Program [(2020)4Y158], Talents of Guizhou Science and Technology Cooperation Platform [(2020)4104], Zunyi Science and Technology Support Program (2023)2, Science and Technology Fund Project of Guizhou Provincial Health Commission (gzwkj2021-445), Zunyi Medical University Graduate Student Research Fund Program (ZYK192, ZYK186, ZYK190).

REFERENCES

(1) Li, X.; Kim, J.; Yoon, J.; Chen, X. Cancer-associated, stimuli-driven, turn-on theranostics for multimodality imaging and therapy. *Adv. Mater.* **2017**, *29*, 1606857.

(2) Gao, M.; Yu, F.; Lv, C.; Choo, J.; Chen, L. Fluorescent chemical probes for accurate tumor diagnosis and targeting therapy. *Chem. Soc. Rev.* **2017**, *46*, 2237−2271.

(3) Wang, Y.; Gong, N.; Li, Y.; Lu, Q.; Wang, X.; Li, J. Atomic-level nanorings (A-NRs) therapeutic agent for photoacoustic imaging and photothermal/photodynamic therapy of cancer. *J. Am. Chem. Soc.* **2020**, *142*, 1735−1739.

(4) Liu, Y. J.; Bhattarai, P.; Dai, Z. F.; Chen, X. Y. Photothermal therapy and photoacoustic imaging via nanotheranostics in fighting cancer. *Chem. Soc. Rev.* **2019**, *48*, 2053−2108.

(5) Yang, Z.; Chen, X. Semiconducting perylene diimide nanostructure: multifunctional phototheranostic nanoplatform. *Acc. Chem. Res.* **2019**, *52*, 1245−1254.

(6) Qi, J.; Ou, H.; Liu, Q.; Ding, D. Gathering brings strength: how organic aggregates boost disease phototheranostics. *Aggregate* **2021**, *2*, 95−113.

(7) Dai, J.; Li, Y.; Long, Z.; Jiang, R.; Zhuang, Z.; Wang, Z.; Zhao, Z.; Lou, X.; Xia, F.; Tang, B. Z. Efficient near-infrared photosensitizer with aggregation-induced emission for imaging-guided photodynamic therapy in multiple xenograft tumor models. *ACS Nano* **2020**, *14*, 854−866.

(8) Nita, M.; Grzybowski, A. The role of the reactive oxygen species and oxidative stress in the pathomechanism of the age-related ocular diseases and other pathologies of the anterior and posterior eye segments in adults. *Oxid. Med. Cell. Longevity* **2016**, *2016*, 3164734.

(9) Dai, J.; Wu, M.; Wang, Q.; Ding, S.; Dong, X.; Xue, L.; Zhu, Q.; Zhou, J.; Xia, F.; Wang, S.; et al. Red blood cell membrane-camouflaged nanoparticles loaded with AIEgen and Poly (I: C) for enhanced tumoral photodynamic- immunotherapy. *Natl. Sci. Rev.* **2021**, *8*, nwab039.

(10) Mu, X.; Tang, Y.; Wu, F.; Ma, H.; Huang, S.; Liang, M.; Yang, J.; Lu, Y.; Zhou, X.; Li, Z. A simple small molecule with synergistic passive and active dual-targeting effects for imaging-guided photothermal cancer therapy. *ACS Appl. Mater. Interfaces* **2021**, *13*, 36958−36966.

(11) Zhu, X.; Feng, W.; Chang, J.; Tan, Y. W.; Li, J.; Chen, M.; Sun, Y.; Li, F. Temperature-feedback upconversion nanocomposite for accurate photothermal therapy at facile temperature. *Nat. Commun.* **2016**, *7*, 10437.

(12) Li, S.; Deng, Q.; Zhang, Y.; Li, X.; Wen, G.; Cui, X.; Wan, Y.; Huang, Y.; Chen, J.; Liu, Z.; et al. Rational design of conjugated small molecules for superior photothermal theranostics in the NIR-II Biowindow. *Adv. Mater.* **2020**, *32*, 2001146.

(13) Wang, Q.; Tian, L.; Xu, J.; Xia, B.; Li, J.; Lu, F.; Lu, X.; Wang, W.; Huang, W.; Fan, Q. Multifunctional supramolecular vesicles for combined photothermal/photodynamic/hypoxia-activated chemotherapy. *Chem. Commun.* **2018**, *54*, 10328−10331.

(14) Zhao, X.; Long, S.; Li, M.; Cao, J.; Li, Y.; Guo, L.; Sun, W.; Du, J.; Fan, J.; Peng, X. Oxygen-dependent regulation of excited-state deactivation process of rational photosensitizer for smart phototherapy. *J. Am. Chem. Soc.* **2020**, *142*, 1510−1517.

(15) Sun, T.; Chen, X.; Wang, X.; Liu, S.; Liu, J.; Xie, Z. Enhanced efficacy of photothermal therapy by combining a semiconducting polymer with an inhibitor of a heat shock protein. *Mater. Chem. Front.* **2019**, *3*, 127−136.

(16) Liu, J. N.; Bu, W.; Shi, J. Chemical design and synthesis of functionalized probes for imaging and treating tumor hypoxia. *Chem. Rev.* **2017**, *117*, 6160−6224.

(17) Li, X.; Jeong, K.; Lee, Y.; Guo, T.; Lee, D.; Park, J.; Kwon, N.; Na, J. H.; Hong, S. K.; Cha, S. S.; et al. Water-soluble phthalocyanines selectively bind to albumin dimers: a green approach toward enhancing tumor-targeted photodynamic therapy. *Theranostics* **2019**, *9*, 6412−6423.

(18) Jung, H. S.; Lee, J. H.; Kim, K.; Koo, S.; Verwilst, P.; Sessler, J. L.; Kang, C.; Kim, J. S. A mitochondria-targeted cryptocyanine-based photothermogenic photosensitizer. *J. Am. Chem. Soc.* **2017**, *139*, 9972−9978.

(19) Jung, H. S.; Verwilst, P.; Sharma, A.; Shin, J.; Sessler, J. L.; Kim, J. S. Organic molecule-based photothermal agents: an expanding photothermal therapy universe. *Chem. Soc. Rev.* **2018**, *47*, 2280−2297.

(20) Cai, H.; Dai, X.; Guo, X.; Zhang, L.; Cao, K.; Yan, F.; Ji, B.; Liu, Y. Ataxia telangiectasia mutated inhibitor-loaded copper sulfide nanoparticles for low-temperature photothermal therapy of hepatocellular carcinoma. *Acta Biomater.* **2021**, *127*, 276−286.

(21) Jiang, A.; Liu, Y.; Ma, L.; Mao, F.; Liu, L.; Zhai, X.; Zhou, J. Biocompatible heat-shock protein inhibitor-delivered flowerlike short-wave infrared nanoprobe for mild temperature-driven highly efficient tumor ablation. *ACS Appl. Mater. Interfaces* **2019**, *11*, 6820−6828.

(22) Liu, H. J.; Wang, M.; Hu, X.; Shi, S.; Xu, P. Enhanced photothermal therapy through the in situ activation of a temperature and redox dual-sensitive nano reservoir of triptolide. *Small* **2020**, *16*, No. e2003398.

(23) Sun, W.; Zhao, X.; Fan, J.; Du, J.; Peng, X. Boron Dipyrromethene nano-photosensitizers for anticancer phototherapies. *Small* **2019**, *15*, No. e1804927.

(24) Luo, S.; Tan, X.; Fang, S.; Wang, Y.; Liu, T.; Wang, X.; Yuan, Y.; Sun, H.; Qi, Q.; Shi, C. Mitochondria-targeted small-molecule fluorophores for dual-modal cancer phototherapy. *Adv. Funct. Mater.* **2016**, *26*, 2826−2835.

(25) Zou, J. H.; Wang, P.; Wang, Y.; Liu, G. Y.; Zhang, Y. W.; Zhang, Q.; Shao, J. J.; Si, W. L.; Huang, W.; Dong, X. C. Penetration depth tunable BODIPY derivatives for pH triggered enhanced photothermal/photodynamic synergistic therapy. *Chem. Sci.* **2019**, *10*, 268−276.

(26) Ye, S.; Rao, J.; Qiu, S.; Zhao, J.; He, H.; Yan, Z.; Yang, T.; Deng, Y.; Ke, H.; Yang, H.; et al. Rational design of conjugated photosensitizers with controllable photoconversion for dually cooperative phototherapy. *Adv. Mater.* **2018**, *30*, 1801216.

(27) Zhao, X.; Dai, Y.; Ma, F.; Misal, S.; Hasrat, K.; Zhu, H.; Qi, Z. Molecular engineering to accelerate cancer cell discrimination and boost AIE-active type I photosensitizer for photodynamic therapy under hypoxia. *Chem. Eng. J.* **2021**, *410*, 128133.

(28) Wang, H.; Wang, Y.; Zheng, Z.; Yang, F.; Ding, X.; Wu, A. Reasonable design of NIR AIEgens for fluorescence imaging and effective photothermal/photodynamic Cancer Therapy. *J. Mater. Chem. B* **2022**, *10*, 1418−1426.

(29) Li, X.; Fang, F.; Sun, B.; Yin, C.; Tan, J.; Wan, Y.; Zhang, J.; Sun, P.; Fan, Q.; Wang, P.; et al. Near-infrared small molecule coupled with rigidness and flexibility for high-performance multimodal imaging-guided photodynamic and photothermal synergistic therapy. *Nanoscale Horiz.* **2021**, *6*, 177−185.

(30) Zheng, J.; Shen, Y.; Xu, Z.; Yuan, Z.; He, Y.; Wei, C.; Er, M.; Yin, J.; Chen, H. Near-infrared off-on fluorescence probe activated by NTR for in vivo hypoxia imaging. *Biosens. Bioelectron.* **2018**, *119*, 141−148.

(31) Xu, A.; Tang, Y.; Ma, Y.; Xu, G.; Gao, S.; Zhao, Y.; Lin, W. A fast-responsive two-photon fluorescent turn-on probe for nitroreductase and its bioimaging application in living tissues. *Sens. Actuators, B* **2017**, *252*, 927−933.

(32) Wang, S.; Liu, Z.; Tong, Y.; Zhai, Y.; Zhao, X.; Yue, X.; Qiao, Y.; Liu, Y.; Yin, Y.; Xi, R.; et al. Improved cancer photo theranostic efficacy of hydrophobic IR780 via parenteral route by association with tetrahedral nanostructured DNA. *J. Controlled Release* **2021**, *330*, 483−492.

(33) Machado, M. G. C.; de Oliveira, M. A.; Lanna, E. G.; Siqueira, R. P.; Pound-Lana, G.; Branquinho, R. T.; Mosqueira, V. C. F. Photodynamic therapy with the dual-mode association of IR780 to PEG-PLA nanocapsules and the effects on human breast cancer cells. *Biomed. Pharmacother.* **2022**, *145*, 112464.

(34) Sun, J.; Hu, Z.; Wang, R.; Zhang, S.; Zhang, X. A highly sensitive chemiluminescent probe for detecting nitroreductase and imaging in living animals. *Anal. Chem.* **2019**, *91*, 1384−1390.

(35) Liu, Z.-R.; Tang, Y.; Xu, A.; Lin, W. A new fluorescent probe with a large turn-on signal for imaging nitroreductase in tumor cells

https://doi.org/10.1021/acsomega.4c03098
ACS Omega 2024, 9, 30685−30697

and tissues by two-photon microscopy. *Biosens. Bioelectron.* **2017**, *89*, 853−858.
(36) Xia, L.; Hu, F.; Huang, J.; Li, N.; Gu, Y.; Wang, P. A fluorescent turn-on probe for nitroreductase imaging in living cells and tissues under hypoxia conditions. *Sens. Actuators, B* **2018**, *268*, 70−76.
(37) Li, Y.; Deng, Y.; Liu, J.; Fu, J.; Sun, Y.; Ouyang, R.; Miao, Y. A near-infrared frequency upconversion probe for nitroreductase detection and hypoxia tumor in vivo imaging. *Sens. Actuators, B* **2019**, *286*, 337−345.
(38) Ding, S.; Yang, M.; Lv, J.; Li, H.; Wei, G.; Gao, J.; Yuan, Z. Novel lysosome-targeting fluorescence off-on photosensitizer for near-infrared hypoxia imaging and photodynamic therapy in vitro and in vivo. *Molecules* **2022**, *27*, 3457.
(39) Li, Y.; Sun, Y.; Li, J.; Su, Q.; Yuan, W.; Dai, Y.; Han, C.; Wang, Q.; Feng, W.; Li, F. Ultrasensitive near-infrared fluorescence-enhanced probe for in vivo nitroreductase imaging. *J. Am. Chem. Soc.* **2015**, *137*, 6407−6416.
(40) Xu, F.; Li, H.; Yao, Q.; Ge, H.; Fan, J.; Sun, W.; Wang, J.; Peng, X. Hypoxia-activated NIR photosensitizer anchoring in the mitochondria for photodynamic therapy. *Chem. Sci.* **2019**, *10*, 10586−10594.
(41) Peng, R.; Yuan, J.; Cheng, D.; Ren, T.; Jin, F.; Yang, R.; Yuan, L.; Zhang, X. Evolving a unique red-emitting fluorophore with an optically tunable hydroxy group for imaging nitroreductase in cells, in tissues, and in vivo. *Anal. Chem.* **2019**, *91*, 15974−15981.
(42) Zhai, B.; Hu, W.; Sun, J.; Chi, S.; Lei, Y.; Zhang, F.; Zhong, C.; Liu, Z. A two-photon fluorescent probe for nitroreductase imaging in living cells, tissues and zebrafish under hypoxia conditions. *Analyst* **2017**, *142*, 1545−1553.
(43) Jiao, Y.; Zhang, L.; Gao, X.; Si, W.; Duan, C. A cofactor-substrate-based supramolecular fluorescent probe for the ultrafast detection of nitroreductase under hypoxic conditions. *Angew. Chem., Int. Ed.* **2020**, *59*, 6021−6027.
(44) Kumar, A.; Deep, G. Hypoxia in tumor microenvironment regulates exosome biogenesis: molecular mechanisms and translational opportunities. *Cancer Lett.* **2020**, *479*, 23−30.
(45) Lin, Q.; Bao, C.; Yang, Y.; Liang, Q.; Zhang, D.; Cheng, S.; Zhu, L. Highly discriminating photorelease of anticancer drugs based on hypoxia activatable phototrigger conjugated chitosan nanoparticles. *Adv. Mater.* **2013**, *25*, 1981−1986.
(46) Biswas, S.; Rajesh, Y.; Barman, S.; Bera, M.; Paul, A.; Mandal, M.; Pradeep Singh, N. D. A dual-analyte probe: hypoxia-activated nitric oxide detection with photo-triggered drug release ability. *Chem. Commun.* **2018**, *54*, 7940−7943.
(47) Cui, L.; Zhong, Y.; Zhu, W. P.; Xu, Y. F.; Du, Q. S.; Wang, X.; Qian, X. H.; Xiao, Y. A New Prodrug-Derived Ratiometric Fluorescent Probe for Hypoxia: High Selectivity of Nitroreductase and Imaging in Tumor Cell. *Org. Lett.* **2011**, *13*, 928−931.
(48) He, L.; Xu, F.; Li, Y.; Jin, H. L.; Lo, P.-C. Cupric-ion-promoted fabrication of oxygen-replenishing nanotherapeutics for synergistic chemo and photodynamic therapy against tumor hypoxia. *Acta Biomater.* **2023**, *162*, 57−71.
(49) Gao, J.; Li, J.; Geng, W. C.; Chen, F. Y.; Duan, X.; Zheng, Z.; Ding, D.; Guo, D. S. Biomarker displacement activation: a general host-guest strategy for targeted phototheranostics in vivo. *J. Am. Chem. Soc.* **2018**, *140*, 4945−4953.
(50) Su, M.; Han, Q.; Yan, X.; Liu, Y.; Luo, P.; Zhai, W.; Zhang, Q.; Li, L.; Li, C. A supramolecular strategy to engineering a non-photobleaching and near-infrared absorbing nano-J-aggregate for efficient photothermal therapy. *ACS Nano* **2021**, *15*, 5032−5042.

https://doi.org/10.1021/acsomega.4c03098
ACS Omega 2024, 9, 30685−30697